Check for updates

Progress in Photovoltaics: Research and Applications

WILEY

PROGRESS IN PHOTOVOLTAICS

RESEARCH ARTICLE OPEN ACCESS

Role of Ag Addition on the Microscopic Material Properties of (Ag,Cu)(In,Ga)Se_2 Absorbers and Their Effects on Losses in the Open-Circuit Voltage of Corresponding Devices

Sinju Thomas[1] | Wolfram Witte[2] | Dimitrios Hariskos[2] | Rico Gutzler[2] | Stefan Paetel[2] | Chang-Yun Song[3] | Heiko Kempa[3] | Matthias Maiberg[3] | Daniel Abou-Ras[1]

[1]Department Structure and Dynamics of Energy Materials, Helmholtz-Zentrum Berlin für Materialien und Energie GmbH, Berlin, Germany | [2]Zentrum für Sonnenenergie- und Wasserstoff-Forschung Baden-Württemberg (ZSW), Stuttgart, Germany | [3]Fachgruppe Photovoltaik, Institut für Physik, Martin-Luther-Universität Halle-Wittenberg, Halle (Saale), Germany

Correspondence: Daniel Abou-Ras (daniel.abou-ras@helmholtz-berlin.de)

Received: 14 December 2023 | **Revised:** 28 May 2024 | **Accepted:** 21 August 2024

Funding: The present work was supported by the Graduate School "MatSEC" and the Bundesministerium für Wirtschaft und Klimaschutz (BMWK)-funded project "EFFCIS-II" under contract numbers 03EE1059A (ZSW), 03EE1059B (HZB), and 03EE1059C (MLU).

Keywords: Cu(In,Ga)Se_2 | grain boundaries | silver | structure–property relationships | thin-film solar cells

ABSTRACT

Ag alloying of Cu(In,Ga)Se_2 (CIGSe) absorbers in thin-film solar cells leads to improved crystallization of these absorber layers at lower substrate temperatures than for Ag-free CIGSe thin films as well as to enhanced cation interdiffusion, resulting in reduced Ga/In gradients. However, the role of Ag in the microscopic structure–property relationships in the (Ag,Cu)(In,Ga)Se_2 thin-film solar cells as well as a correlation between the various microscopic properties of the polycrystalline ACIGSe absorber and open-circuit voltage of the corresponding solar cell device has not been reported earlier. In the present work, we study the effect of Ag addition by analyzing the differences in the various bulk, grain-boundary, optoelectronic, emission, and absorption-edge properties of ACIGSe absorbers with that of a reference CIGSe absorber. By comparing thin-film solar cells with similar band-gap energies ranging from about 1.1 to about 1.2 eV, we were able to correlate the differences in their absorber material properties with the differences in the device performance of the corresponding solar cells. Various microscopic origins of open-circuit voltage losses were identified, such as strong Ga/In gradients and local compositional variations within individual grains of ACIGSe layers, which are linked to absorption-edge broadening, lateral fluctuations in luminescence-energy distribution, and band tailing, thus contributing to radiative V_{OC} losses. A correlation established between the effective electron lifetime, average grain size, and lifetime at the grain boundaries indicates that enhanced nonradiative recombination at grain boundaries is a major contributor to the overall V_{OC} deficit in ACIGSe solar cells. Although the alloying with Ag has been effective in increasing the grain size and the effective electron lifetime, still, the Ga/In gradients and the grain-boundary recombination in the ACIGSe absorbers must be reduced further to improve the solar-cell performance.

1 | Introduction

Thin-film solar cells with Cu(In,Ga)Se_2 (CIGSe) absorbers have reached a record conversion efficiency of 23.6%, which was achieved with Ag-alloyed CIGSe (ACIGSe) absorber layers [1]. The addition of Ag allows for the formation of ACIGSe layers at lower deposition temperatures owing to the smaller formation enthalpy of the Ag-containing CIGSe phase [2]. Larger crystallites are formed upon Ag addition owing to higher crystallization rates, resulting from lower energy barriers for ACIGSe

This is an open access article under the terms of the Creative Commons Attribution License, which permits use, distribution and reproduction in any medium, provided the original work is properly cited.

© 2024 The Author(s). Progress in Photovoltaics: Research and Applications published by John Wiley & Sons Ltd.

formation compared with that of CIGSe [3]. Therefore, more energy is available for crystallization, leading to ACIGSe absorber layers with larger average grain sizes than in Ag-free CIGSe absorber layers grown at the same substrate temperature on the same substrate [3–5]. Also, in addition, Ag alloying of CIGSe thin films results in stronger interdiffusion of cations. This leads to relatively less pronounced Ga/In gradients in ACIGSe layers; thus, correspondingly, radiative losses of the open-circuit voltage V_{OC} are decreased [6].

Although the effect of Ag alloying on some microstructural properties in ACIGSe layers (e.g., on the average grain size) has already been reported, it is still important to understand the role of Ag alloying in improving the device performance. An in-depth analysis of the effect of Ag alloying on the microscopic material properties of the CIGSe absorbers and their effect on the device performance has not been performed so far. Therefore, it is necessary to conduct a systematic analysis of the microscopic structure–property relationships in the ACIGSe photoabsorbers and corresponding solar cells. There is no established link connecting the microstructure as well as further microscopic material properties of the absorber with the macroscopic device performance, which is limited to a large degree by V_{OC} losses of the thin-film solar cell.

The present work intends to fill this gap by investigating one reference CIGSe thin-film solar cell without Ag and four ACIGSe thin-film solar cells with [Ag]/([Ag] + [Cu]) (AAC) ratios of 0.05 and 0.14; although substantial characterization efforts were invested, we still highlight the limited statistical relevance. We aim to track the changes in material properties on the microscopic scale by comparing the reference CIGSe thin-film solar cell and the ACIGSe thin-film solar cells. This is carried out by employing various scanning electron microscopy (SEM) methods on the identical areas of cross-sectional specimens, in addition to time-resolved photoluminescence (TRPL) and external quantum efficiency (*EQE*) measurements on the (A)CIGSe thin-film solar cells. It was found that CIGSe absorbers with and without Ag exhibit differences in their material properties that can be linked to the differences in the device performance of the corresponding solar cells.

2 | Materials and Methods

CIGSe and ACIGSe solar cells were fabricated following a standardized production workflow; see [7] for further details. A Mo layer with a thickness of approximately 550 nm was sputtered onto soda-lime glass (SLG) substrates. The CIGSe and ACIGSe absorbers, about 2200 nm thick, were co-evaporated using an industry-scale $30 \times 30\,cm^2$ inline coater. The temperature of the substrate heater during the absorber deposition was set to 700°C for the CIGSe film (cell #2) as well as to 650°C (cell #3) and 580°C (cells #1, #4, and #5) for ACIGSe films. Each temperature for CIGSe and ACIGSe is optimized for best device performance. The CGI and ACGI ratios were adjusted by controlling the Cu and Ag evaporator temperatures, though the growth duration remained constant. All samples underwent an in situ RbF post-deposition treatment without breaking the vacuum. The CIGSe sample was treated at a higher RbF-source temperature of 530°C, and the ACIGSe samples were treated with less RbF-source temperatures of 510–520°C to result in best cell efficiencies. Chemical bath deposition was employed to grow around 50-nm-thick CdS buffer layers to have a broad process window. On top of the buffer layer, a ZnO layer was sputtered. Subsequently, a 280-nm-thick Al-doped ZnO (AZO) layer was deposited via direct-current sputtering as the front contact at a substrate temperature of 200°C. All steps, except for buffer deposition using a chemical bath, were performed as inline processes. Finally, a Ni/Al/Ni grid was deposited using electron-beam evaporation, and the cells were defined with a $0.5\,cm^2$ total area by means of mechanical scribing and feature no anti-reflective coating.

Solar cell parameters were measured using a WACOM AM1.5G solar simulator at standard testing conditions. We used a four-point geometry and a silicon reference solar cell for calibration. TRPL was used to measure the lifetime of the minority charge carriers. A photomultiplier detector (H10330A-45, PMA-C) and a diode laser with a wavelength and frequency of 640 nm and 1 MHz were used in this experiment. After etching using diluted HCl solutions, the TRPL signals were recorded on the bare CIGSe absorber layer at room temperature.

The drive-level capacitance profiling (DLCP) measurements were conducted at a constant temperature of 300 K using an Agilent E4980A precision LCR meter. A bias voltage was applied, ranging from 0.5 to −1.2 V with an amplified-current amplitude variation from 0.03 to 0.33 V. Before the measurements, the solar cells were exposed to light soaking under white light, followed by a transition to a dark state for the actual data acquisition. Further details on this technique can be found in [8].

The E_g values were calculated from the mean values (peak energies) of the first derivatives of the *EQE* d(*EQE*)/d*E* dependencies following the approach described in [9, 10]. The Urbach energies E_U were determined from the sub-gap region of the *EQE* spectra based on the approach outlined in [11]. The *EQE* spectra were acquired on ACIGSe and CIGSe solar cells over a wavelength range of 300–1400 nm. An illumination spot size of $5 \times 5\,mm^2$ and a grating monochromator were used for recording the *EQE* spectra at a step size for the wavelength of 10 nm. Silicon and indium-gallium-arsenide solar cells were used for the references.

A Zeiss UltraPlus scanning electron microscope equipped with a Symmetry electron backscatter diffraction (EBSD) camera and an Ultim Extreme energy-dispersive x-ray spectroscopy (EDS) detector (both by Oxford Instruments) were used for the acquisition of corresponding maps on polished cross sections. Two stripes of each solar cell were glued face-to-face together using an epoxy glue, and then the cross-section surface was polished mechanically and using and Ar-ion beam (see [12] for more details). The acquisition and evaluation of the EBSD and EDS maps was performed by means of the software suite AZtec. The EDS maps were measured at an acceleration voltage of 7 kV. To determine the GGI profiles, the elemental concentrations were estimated from the net counts in the EDS maps using the integral compositions from XRF measurements. The EBSD measurements were performed at a beam energy of 15 keV and at a step size of 50 nm. A pseudocubic symmetry was used for the indexing of the EBSD patterns. A Zeiss Merlin scanning electron microscope equipped with a DELMIC SPARC cathodoluminescence (CL) system was

1099159x, 2024, 12, Downloaded from https://onlinelibrary.wiley.com/doi/10.1002/pip.3845 by Helmholtz-Zentrum Berlin Für, Wiley Online Library on [12/12/2024]. See the Terms and Conditions (https://onlinelibrary.wiley.com/terms-and-conditions) on Wiley Online Library for rules of use; OA articles are governed by the applicable Creative Commons License

used for acquiring hyperspectral images. CL images were acquired at an acceleration voltage of 10 kV and at a beam current of 1.2 nA and were evaluated using the DELMIC Odemis viewer as well as the Fiji software tool.

3 | Results

3.1 | Device Performance and Absorber Compositions of Individual ACIGSe Thin-Film Solar Cells

Table 1 shows the [Ag]/([Ag]+[Cu]) (AAC), ([Ag]+[Cu])/([Ga]+[In]) (ACGI), [Ga]/([Ga]+[In]) GGI of the ACIGSe absorbers and the photovoltaic parameters of the corresponding thin-film solar cells. The overall solar-conversion efficiency (η) decreases from 18.5 to 15.7% with increasing E_g (determined from the mean of d*EQE*/d*E*). The fill factor (*FF*) of the five solar cells does not exhibit a strong variation with one another and remains at about 78%. The short-circuit current density (j_{sc}) slightly decreases from 33 (cell #1) to 30 mA/cm^2 (cell #5) with E_g increasing from 1.1 to 1.2 eV, in agreement with the Shockley–Queisser (SQ) theory [13]. In contrast to the SQ assumption, there is a decrease in V_{OC} with respect to E_g and the V_{OC} deficit ($\Delta V_{OC} = E_g/q - V_{OC}$) steadily increases from cell #1 to cell #5. Cell #2 with AAC = 0 (Ag-free CIGSe) is the reference cell. Although ACIGSe thin-film solar cells #1 and #2 exhibit nearly identical E_g of 1.13–1.15 eV, their V_{OC} is different, and the same is the case with solar cells #3, #4, and #5 where $E_g \sim 1.2$ eV (1.19–1.21 eV), but they exhibit a larger difference in the V_{OC}. We note that an important contributing factor to the difference in the conversion efficiencies is the difference in the ACGI ratios between the samples. In order to understand the reason for the variation in V_{OC} and for the deviation from SQ theory from the microscopic material properties point of view, as well as to elucidate the role of the Ag alloying to CIGSe, a comparison of the various material properties of the ACIGSe absorbers in these thin-film solar cells with nearly identical E_g (with and without Ag) will be shown in the following sections.

3.2 | Material Properties of ACIGSe Absorbers in Completed Solar Cells

In the present work, we divided the ACIGSe thin-film solar cells into two groups: Group 1 (two cells #1 and #2) with E_g of about 1.13–1.15 eV and Group 2 (three cells #3–#5) with E_g of about 1.19–1.21 eV. Despite (nearly) the same E_g, the solar cells exhibit considerably different V_{OC} values. In the following, we will compare the various material properties of the CIGSe and ACIGSe photoabsorbers in order to understand the origins of V_{OC} deficits in each of these solar cells, that is, #1–#2 and #3–#5. We note that the net-doping densities determined by DLCP exhibited a trend already reported by other authors [6, 14, 15], that is, decreasing net-doping density with increasing AAC (range about 9×10^{15} to 9×10^{14} cm^{-3}; see Table S6).

Three categories of material properties will be considered: firstly, microstructural, compositional, and optoelectronic properties; secondly, the absorption edge and emission characteristics; and lastly, the effective electron lifetime as well as the recombination at GBs. As the effective electron lifetimes in the (A)CIGSe layers were determined on (A)CIGSe/Mo/glass stacks, that is, without the ZnO:Al/i-ZnO/CdS contact layers, we do not discuss recombination at the CdS/(A)CIGSe interface in the present work.

3.2.1 | Microstructural, Compositional, and Luminescence Properties

3.2.1.1 | Group 1 (Cells #1 and #2) With $E_g \sim 1.13$–1.15 eV and AAC = 0.05 and 0. Figure 1 depicts a comparison of the microstructures from EBSD maps (Figure 1b,g), the Ga distributions via EDS (Figure 1c,h), as well as the spatial distributions of the CL intensity and peak energy (Figure 1d,e,i,j) of the cell with AAC = 0.05 and of the reference cell with AAC = 0. EBSD maps shown in Figure 1b,g are representative maps from each 10 of such EBSD maps acquired on neighboring regions. No strong film textures of the polycrystalline ACIGSe absorbers were detected (Figure S1). The average grain sizes d_{grain} in the ACIGSe and CIGSe layers were extracted by assuming a Gaussian distribution over 200 grains (we note that this approach is simplified, as grain sizes in CIGSe/ACIGSe thin films exhibit lognormal, not Gaussian, distributions [16]).

The ACIGSe absorber of cell #1 is composed of larger grains of $d_{grain} = 1\,\mu$m than those of cell #2 without any Ag ($d_{grain} = 0.7\,\mu$m). Relatively smaller d_{grain} in cell #2 indicates higher GB density than cell #1. Although the size of the grains does not strongly vary from the CdS/ACIGSe interface to the Mo back-contact, the EDS maps of the Ga signal in Figure 1c,h indicate significant Ga gradients in the absorbers of both cells. The line scans in Figure 2a,b extracted perpendicular to the substrate (highlighted in white-dashed rectangle) from

TABLE 1 | Photovoltaic parameters and V_{OC} deficits (ΔV_{OC}) of the four ACIGSe and one Ag-free CIGSe solar cell with different [Ag]/([Ag]+[Cu]) (AAC), ([Ag]+[Cu])/([Ga]+[In]) (ACGI), and [Ga]/([Ga]+[In]) (GGI) ratios (determined via XRF) and almost similar bandgap energies (E_g) determined from the energetic onsets in *EQE* spectra. The photovoltaic parameters are those of the best device of each sample (stripe with 10 cells).

Cell no.	AAC	ACGI	GGI	E_g (eV)	η (%)	*FF* (%)	j_{sc} (mA/cm^2)	V_{OC} (mV)	ΔV_{OC} (mV)
#1	0.05	0.85	0.29	1.13	18.4	79	33	719	411
#2	0.00	0.81	0.32	1.15	18.5	79	32	726	424
#3	0.14	0.81	0.29	1.19	17.5	79	31	714	476
#4	0.05	0.72	0.34	1.20	16.5	77	31	677	523
#5	0.14	0.68	0.34	1.22	15.7	78	30	664	556

1099159x, 2024, 12, Downloaded from https://onlinelibrary.wiley.com/doi/10.1002/pip.3845 by Helmholtz-Zentrum Berlin Für, Wiley Online Library on [12/12/2024]. See the Terms and Conditions (https://onlinelibrary.wiley.com/terms-and-conditions) on Wiley Online Library for rules of use; OA articles are governed by the applicable Creative Commons License

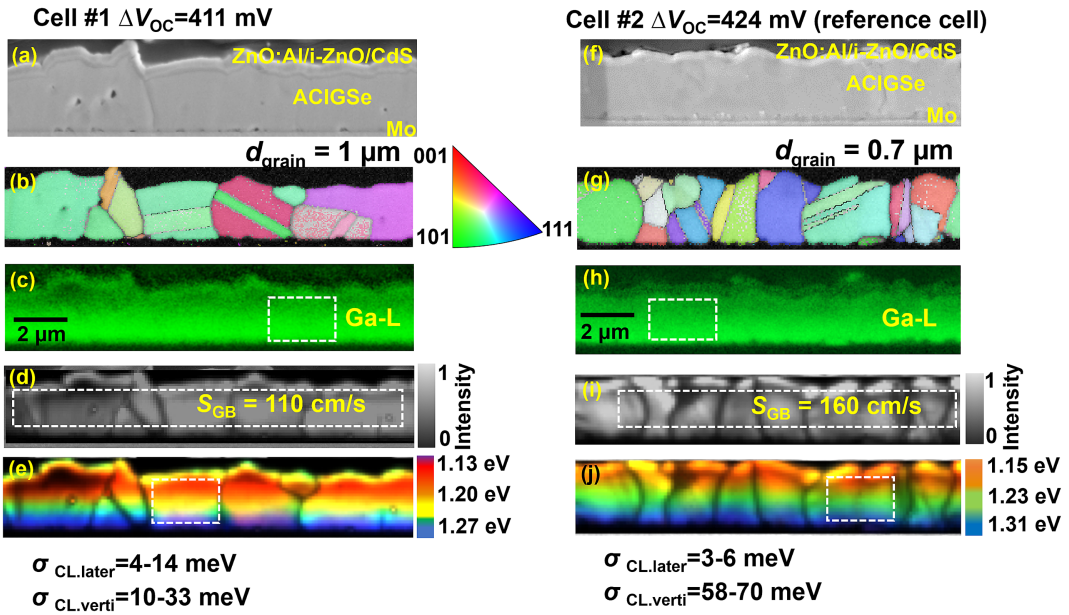


FIGURE 1 | Various microscopic results from the identical specimen areas on the cross sections of the ACIGSe and CIGSe absorbers of the cells #1 and #2, prepared from ZnO/CdS/ACIGSe/Mo/glass stacks. (a,f) SEM images. (b,g) EBSD pattern-quality maps, showing the differences in the grain sizes. (c,h) Ga distribution maps (Ga-L x-ray lines) obtained via EDS. The highlighted regions (white dashed rectangles) indicate the areas from where the linescans perpendicular to the substrate were extracted (Figure 2). (d,i) CL intensity distributions. The white dashed rectangles indicate the regions in which GB recombination velocities were determined. (e,j) CL emission-energy distribution map. The white dashed rectangles indicate the regions from which the fluctuations in the CL peak energy distributions were calculated.

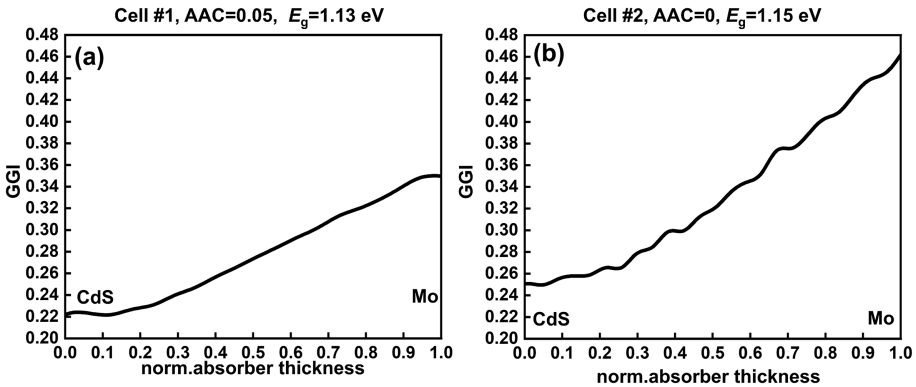


FIGURE 2 | GGI gradients extracted from the EDS maps of the absorbers. (a) GGI gradient for cell #1, $E_g = 1.13$ eV. (b) GGI gradient for cell #2, $E_g = 1.15$ eV.

the EDS map confirms a pronounced local variation in composition within individual grains in the CIGSe and ACIGSe layers. The CIGSe absorber of cell #2 with AAC = 0 exhibits a stronger GGI gradient varying from GGI = 0.25 to 0.46 towards the back-contact when compared with that of cell #1 with AAC = 0.05, in which the GGI varies over a smaller range between 0.22 and 0.33. For all (A)CIGSe layers, [Ga] is slightly enhanced at the (A)CIGSe surface (see Figure S2.2). Whereas Se exhibits homogeneous elemental distributions across the ACIGSe layers, the Ag (Cu) concentration is maximum (minimum) close to the CdS/ACIGSe (ACIGSe/Mo) interface and decreases (increases) towards the ACIGSe/Mo (CdS/ACIGSe) interface for all ACIGSe layers (Figure S2.3; the reader is referred to Table S3 for the integral concentrations of the constituent elements). Such elemental distributions have been reported before; for example, Sopiha et al. suggested that these AAC gradients are thermodynamically driven [17].

However, microstrain should be considered as strong driving force for the detected interdiffusion of cations in the ACIGSe lattice. A first origin of microstrain results from the fact that Ga–Se and Cu–Se bonding lengths in the tetragonal (A)CIGSe structure are quite similar [18], whereas In–Se and Cu–Se bonds differ substantially [19]; the corresponding microstrain can be reduced by driving In ions towards the film surface. Moreover, $AgInSe_2$ and $AgGaSe_2$ lattices exhibit distorted bonds [20, 21], that is, alloying CIGSe with Ag introduces a second origin of microstrain, leading to a preferential segregation of Ag to the film surface. The resulting Ag/Cu and Ga/In gradients perpendicular to the substrate are equilibria of the

1099159x, 2024, 12, Downloaded from https://onlinelibrary.wiley.com/doi/10.1002/pip.3845 by Helmholtz-Zentrum Berlin Für, Wiley Online Library on [12/12/2024]. See the Terms and Conditions (https://onlinelibrary.wiley.com/terms-and-conditions) on Wiley Online Library for rules of use; OA articles are governed by the applicable Creative Commons License

two strain mechanisms described above and naturally depend on the integral AAC and GGI ratios in a given ACIGSe layer, as shown by Sopiha et al. [17].

The CL intensity distributions in Figure 1d,i feature higher luminescence intensity at the grain interiors and towards the CdS buffer and a decreased intensity at the GBs and towards the Mo back-contact. More specifically, for all (A)CIGSe layers, at the surface-near regions that exhibited a slight enrichment in Ga, the CL intensities are maximum, and the peak energy is about 1.3 eV (an exemplary CL intensity map with extracted profile perpendicular to the substrate for cell #1 is given in Figure S8). Based on the measured data, it is not possible to conclude on the specific phase of this ACIGSe-surface layer.

A decrease in intensity at the GBs is an indication of enhanced nonradiative recombination at these planar defects. However, the intensity variation from the CdS buffer to the Mo back-contact is related also to the GGI and E_g gradient perpendicular to the substrate. The CL intensity is higher near the regions with smaller GGI/E_g (towards the CdS buffer) owing to enhanced generation and recombination of electron–hole pairs. Owing to the higher GGI/E_g towards the back-contact, the CL intensity is relatively lower in this region. The luminescence-energy distribution in Figure 1e,j exhibit increases in the CL peak energy from the ACIGSe/CdS to the Mo/ACIGSe interfaces, which further confirms the EDS results highlighting E_g gradients in the absorbers perpendicular to the substrates.

3.2.1.2 | Group 2 (Cells #3, #4, and #5) With E_g ~1.2 eV. Figure 3 gives a comparison of various microscopic properties of the ACIGSe absorbers of the three cells whose ΔV_{OC} values vary from 476 to 556 mV (Table 1) with different AAC ratios. The EBSD results (Figure 3b,g,l) show that the ACIGSe absorber of cell #3 has a much larger average grain size of $d_{grain} \approx 4.7\,\mu m$ than those of the ACIGSe layers in cells #4 and #5 with $d_{grain} = 0.8$; we note that this result is probably due to the higher substrate temperature for the ACIGSe layer in cell #3 (650°C) than for those in cells #4 and #5 (580°C). It can be seen in the EBSD maps (particularly for cells #3 and #5) that many individual grains extend across the entire ACIGSe film thickness from the CdS buffer to the Mo back-contact.

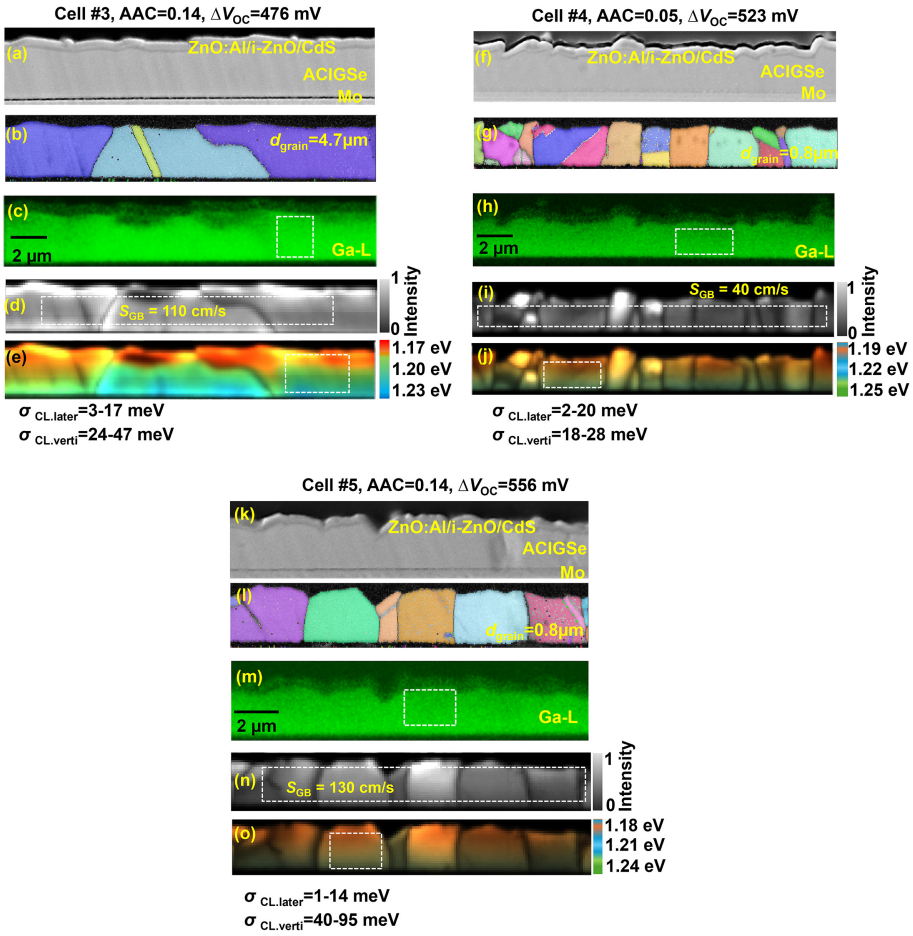


FIGURE 3 | Various microscopic results from the identical specimen areas on the cross sections of the ACIGSe absorbers of the cells #3, #4, and #5, prepared from ZnO/CdS/CIGSe/Mo/glass stacks. (a,f,k) SEM images. (b,g,l) EBSD pattern-quality maps, showing the differences in the grain sizes. (c,h,m) Ga distribution maps (Ga-L x-ray lines) obtained via EDS. The highlighted regions (white dashed rectangles) indicate the areas from where the line scans perpendicular to the substrate were extracted. (d,i,n) CL intensity distributions. The white dashed rectangles indicate the regions in which GB recombination velocities were determined. (e,j,o) CL emission-energy distributions. The white dashed rectangles indicate the regions from which the fluctuations in the CL peak energy distributions were calculated.

1099159x, 2024, 12, Downloaded from https://onlinelibrary.wiley.com/doi/10.1002/pip.3845 by Helmholtz-Zentrum Berlin Für, Wiley Online Library on [12/12/2024]. See the Terms and Conditions (https://onlinelibrary.wiley.com/terms-and-conditions) on Wiley Online Library for rules of use; OA articles are governed by the applicable Creative Commons License

The Ga distributions in Figure 3c,h,m exhibit strong Ga gradients within the individual grains. The ACIGSe absorbers of cells #3 and #5 (Figure 4a,c) with each an AAC ratio of 0.14 feature less pronounced Ga/In gradients when compared with the GGI gradient of cell #4 (Figure 4b) with a smaller AAC of 0.05. This result indicates that the higher [Ag] in the ACIGSe absorbers in cells #3 and #5 reduces the gradient of the ACIGSe absorber. Nevertheless, the slopes of the gradients, given by GGI vs. distance, are very similar to one another in the absorber layers (Figures 2 and 4).

The EDS maps of the other constituent elements in the ACIGSe layers such as Ag, Cu, In, and Se are provided in Figure S2.1. Ga depletion in the ACIGSe layer near the CdS buffer is visible for cell #3 (Figure 3c), which does not indicate any secondary phase. However, the CL intensity and the CL peak energy is decreased in this region (Figure 3d,e). The spatial distributions of the luminescence intensity of the three cells (Figure 3d,i,n) exhibit a decrease in the CL intensity at the GBs, indicating enhanced nonradiative recombination at these planar defects. The CL peak energies (Figure 3e,j,o) of the three ACIGSe absorbers are distributed perpendicular to the substrate in a way that it agrees well with the GGI and E_g gradients depicted in Figure 4a–c.

3.2.2 | Absorption-Edge and Spatial Luminescence Characteristics

The broadening of the absorption-edge onset, σ_{total}, as well as the Urbach energies E_U (Table 2) were determined from the *EQE* spectra acquired on cells #1 to #5 following the approach described in [9–11]. The E_g extracted from the *EQE* is in good agreement with the E_g calculated from the minimum/effective GGI of the GGI gradients using the relation in [22]. The standard deviation (σ_{total}) of the first derivative of *EQE* d (*EQE*)/d*E* is connected to radiative V_{OC} losses (ΔV_{OC}^{rad}) via $\Delta V_{OC}^{rad} = \sigma^2_{total}/2k_BT$ [10], where k_B is Boltzmann constant and T is the absolute temperature. Although in [10], it is outlined that $\sigma^2_{total}/2k_BT$ exhibits contributions also from other thermally activated recombination mechanisms, in the present work, we attribute this quantity to radiative recombination only.

The *EQE* spectra for the five (A)CIGSe solar cells are given in Figure S4. We do not attempt to disentangle the broadening σ_{total} with respect to the material properties, as done in a previous work [23]. All the ACIGSe thin-film solar cells exhibit a high σ_{total} of approximately 50 meV, independent of their AAC, thus contributing correspondingly to substantial radiative V_{OC} losses (Table 2). This similarity in the magnitude of σ_{total} values can be attributed to the GGI gradients in all the five ACIGSe absorbers that exhibit similar linear patterns and slopes (from CdS to Mo), due to which their effects on the *EQE* onsets of the corresponding thin-film solar cells are also similar. E_U increases with E_g from 14 to 28 meV from cells #1 to #5, which indicates an additional contribution to the overall ΔV_{OC} from enhanced nonradiative recombination via extended defect states.

The ratios of lattice constants c/a were calculated from the alloy compositional ratios AAC, GGI, and ACGI for the individual ACIGSe thin-film solar cells using equations given in [4]; with respect to the Ga/In and Ag/Cu gradients present in the (A)CIGSe layers (see EDS results above), we note that these c/a ratios are averages using the integral compositions. A general trend is apparent in the Urbach energy E_U, which is larger with larger deviation in c/a from the pseudocubic point (c/a = 2). This result can be explained by the fact that as much as lattice

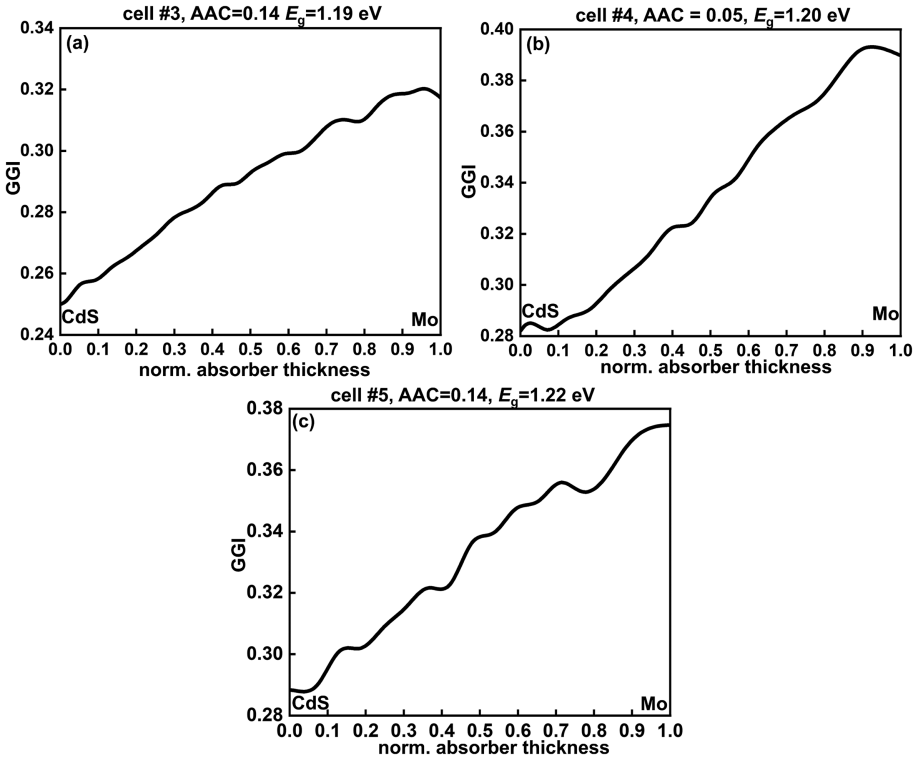


FIGURE 4 | GGI gradients extracted from the EDS maps of the ACIGSe absorbers. (a) GGI gradient for cell #3, $E_g = 1.19$ eV. (b) GGI gradient for cell #4, $E_g = 1.20$ eV. (c) GGI gradient for cell #5, $E_g = 1.22$ eV.

1099159x, 2024, 12, Downloaded from https://onlinelibrary.wiley.com/doi/10.1002/pip.3845 by Helmholtz-Zentrum Berlin Für, Wiley Online Library on [12/12/2024]. See the Terms and Conditions (https://onlinelibrary.wiley.com/terms-and-conditions) on Wiley Online Library for rules of use; OA articles are governed by the applicable Creative Commons License

TABLE 2 | Band-gap energy (E_g), absorption-edge broadening (σ_{total}), and Urbach energy (E_U) determined from *EQE* spectra, as well as the structural deviation from pseudocubic point, |c/a − 2| (determined from the integral compositional ratios obtained via x-ray fluorescence analysis), the fluctuations in the CL energy distribution parallel ($\sigma_{later.CL}$) and perpendicular ($\sigma_{verti.CL}$) to the substrate, and the radiative V_{OC} deficit ΔV_{OC}^{rad}, determined for cells #1 to #5.

Cell no.	E_g (eV)	σ_{total} (meV)	E_U (meV)	|c/a-2|	$\sigma_{later.CL}$ (meV)	$\sigma_{verti.CL}$ (meV)	ΔV_{OC}^{rad} (mV)
#1	1.13	51	14	0.007	4–14	10–33	52
#2	1.15	47	17	0.006	3–6	58–70	44
#3	1.19	46	18	0.012	3–17	24–47	42
#4	1.20	57	21	0.010	2–20	18–28	65
#5	1.22	49	28	0.016	1–14	40–95	48

distortions, that is, microstrain, affect the crystal lattice in real space, they also modify the density of (defect) states in the reciprocal space, which in the photon-energy region of (closely) below E_g are represented by the Urbach tail.

The absorption features σ_{total} and E_U, apparently linked to local variations in alloy compositions and microstrain, can be related to lateral inhomogeneities in the luminescence emission of the absorbers. The fluctuations in the CL peak energy distributions were obtained from calculating the standard deviation of the CL energy across 30 pixels in directions both parallel ($\sigma_{later.CL}$) and perpendicular ($\sigma_{verti.CL}$) to the substrate (highlighted regions in Figure 1e,j, as well as in Figure 2e,j,o). The different standard deviations obtained within each line or column of pixels are given as ranges for $\sigma_{later.CL}$ and $\sigma_{verti.CL}$ in Table 2. The range of $\sigma_{later.CL}$ in cell #2 is roughly similar to that of cell #1, which agrees with similar |c/a − 2| and σ_{total} values. In contrast, $\sigma_{verti.CL}$ of cell #2 is much higher than that of cell #1, probably due to the more pronounced GGI gradient.

When comparing the fluctuations in the CL-peak energy distribution of cells #3, #4, and #5, there is no pronounced variation in the $\sigma_{later.CL}$ of these cells. $\sigma_{verti.CL}$ is the highest for the ACIGSe absorber of cell #5 that also exhibits the largest deviation in c/a from the pseudocubic point. The various $\sigma_{verti.CL}$ values for these three cells correlate with their varying |c/a − 2|.

3.2.3 | Electron Lifetime and Recombination at GBs

Linescans (see Figure S7 as an example) were extracted from CL intensity distributions perpendicular to GB planes (highlighted regions in Figure 1d,i as well as in Figure 2d,i,n) in order to quantify the recombination velocities at the GBs. We applied the approach proposed by Mendis et al. [24], for which the logarithm of the CL intensity gradient $\ln[\Delta I(x)]$ is fitted with a linear function $\ln[S/(S+1)] - x/L$ (x being the position of the electron beam, L the electron diffusion length, and S the reduced recombination velocity with $S = S_{GB}\,\tau_{bulk}/L$). This approach has been applied successfully to CIGSe absorbers [25–27]. A value for τ_{bulk} is required to calculate the recombination velocity S_{GB}. In order to obtain τ_{bulk} indirectly, we first estimated the effective electron lifetimes (τ_{eff}) from the TRPL decays. TRPL measurements were acquired on the CIGSe and ACIGSe absorbers immediately after etching using a diluted HCl solution (Figure 5a–e, red). The TRPL curves featured two sections, one with a faster decay time τ_1 and one with a slower decay time τ_2. τ_{eff} was calculated for each of the CIGSe and ACIGSe absorbers by fitting the corresponding TRPL decay using a bi-exponential function [28] of the form $y(x) = A_1\ \exp(x/\tau_1) + A_2\ \exp(x/\tau_2)$ (red lines in Figure 5a–e). The weighted average of both the lifetimes gives the effective lifetime as $\tau_{eff} = [A_1/(A_1 + A_2)]\tau_1 + [A_2/(A_1 + A_2)]\tau_2$. To judge the injection conditions during the TRPL analyses, the laser intensity was varied. The τ_{eff} values decrease or rather saturate with increasing intensity (as expected when moving from low-injection to high-injection conditions); therefore, we selected the τ_{eff} values obtained at the lowest laser intensity (see Table S5 for details).

As visible from Figure 2, the region of the lowest band-gap energy where the luminescence is most effective is situated closer to the CIGSe surface. Hence, the PL decay does not include any influence from the CIGSe/Mo back interface recombination. As the recombination at the front interface is not investigated in the present work, we use a simplified approximation of Matthiessen's rule and express the inverse of τ_{eff} using the inverse values of τ_{bulk} and τ_{GB} [29]:

$$\tau_{eff}^{-1} = \tau_{bulk}^{-1} + \tau_{GB}^{-1} \tag{1}$$

Here, $\tau_{bulk}^{-1} = \tau_{bulk,rad}^{-1} + \tau_{bulk,nonrad}^{-1}$ ($\tau_{bulk,rad}$ and $\tau_{bulk,nonrad}$ are the radiative and nonradiative parts of the total bulk lifetime), and τ_{GB} is the GB lifetime of electrons (i.e., enhanced nonradiative recombination via point defects at the GB plane). Moreover, $\tau_{bulk,rad} >> \tau_{bulk,nonrad}$; therefore, $\tau_{bulk}^{-1} \sim \tau_{bulk,nonrad}^{-1}$. Note that τ_{bulk} contains significant contributions from recombination at the CIGSe surface. Several factors such as carrier detrapping and lateral inhomogeneities may also have an effect on the TRPL decay [30]. As a result, considerable error bars in both the estimated bulk lifetimes and the corresponding GB lifetimes that are of the same order of magnitude as the estimated values have to be taken into account.

Two boundary conditions were used for estimating τ_{bulk}. Firstly, the $S_{GB,0}$ calculated from an assumed τ_{bulk} must satisfy the following equation (that relates the τ_{GB}, $S_{GB,0}$, and d_{grain}) in addition that the calculated $\tau_{GB} \geq \tau_{eff}$ [31–34];

$$\tau_{GB} = d_{grain} / (6 - n) S_{GB,0} \tag{2}$$

1099159x, 2024, 12, Downloaded from https://onlinelibrary.wiley.com/doi/10.1002/pip.3845 by Helmholtz-Zentrum Berlin Für, Wiley Online Library on [12/12/2024]. See the Terms and Conditions (https://onlinelibrary.wiley.com/terms-and-conditions) on Wiley Online Library for rules of use; OA articles are governed by the applicable Creative Commons License

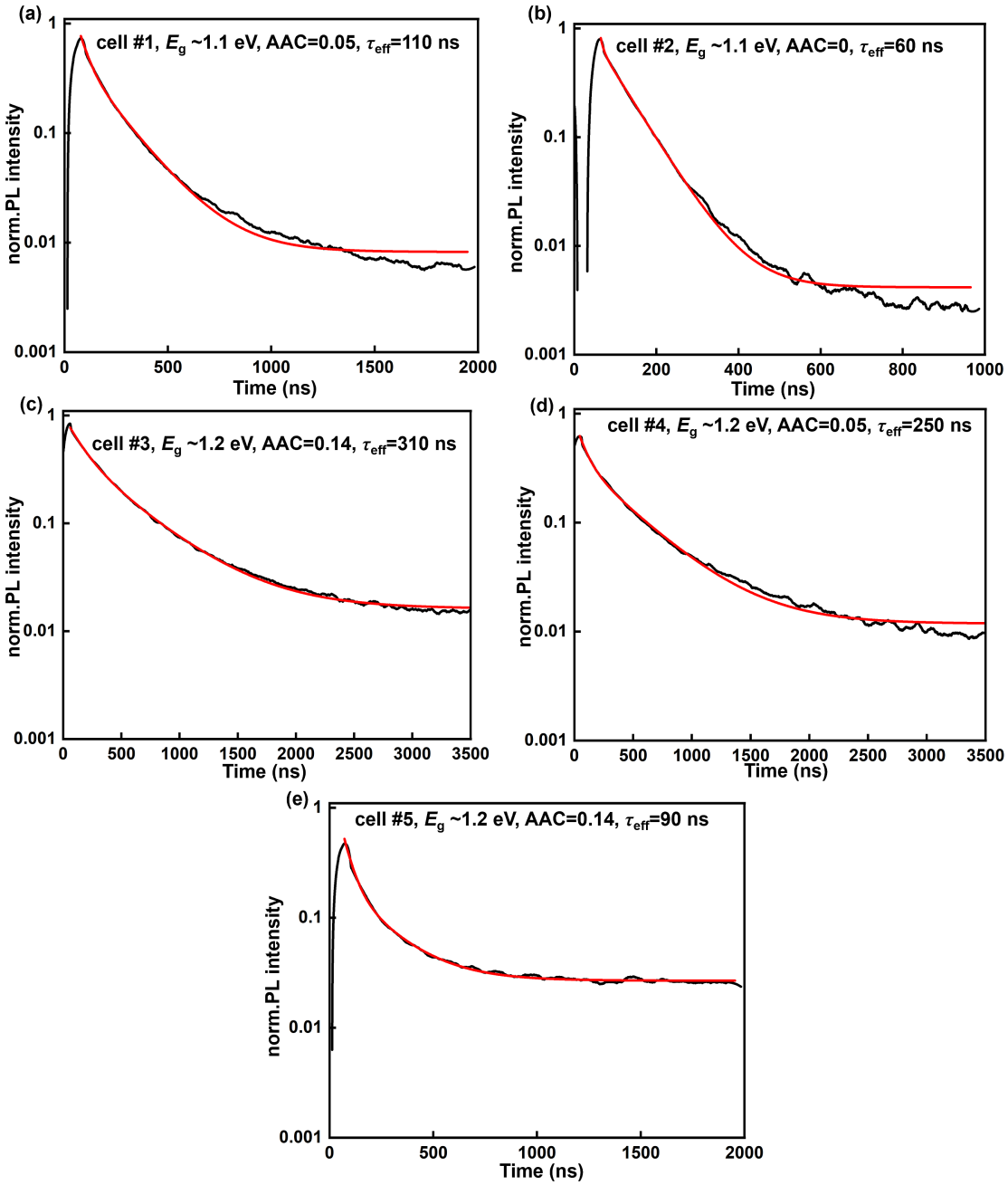


FIGURE 5 | (a,b) TRPL decays (black curves) for ACIGSe and CIGSe solar cells #1 and #2. τ_{eff} decreases from 110 to 60 ns. (c–e) TRPL decays (black curves) for ACIGSe solar cells #3, #4, and #5. τ_{eff} decreases from 310 to 90 ns. The curves in red color are the bi-exponential fit curves. We note that the maximum PL intensities are not exactly 1 (note the logarithmic scales of the y axes) as the TRPL signals were smoothened before the fitting procedures.

We assume the grain to be of a cubical shape with six faces. In the present work, the extent of passivation at the interfaces and GBs is not determined; hence, the number of passivated faces is set $n=0$. When applying the approach described above, GB recombination velocities S_{GB} were determined across 20 different GBs in each of the five (A)CIGSe absorbers.

The recombination velocity S_{GB} can be approximated by $N_{GB}\,\sigma_{GB}\,v_{th}\,\exp(-\Phi_B/k_BT)$ [34], where N_{GB} and σ_{GB} are the effective point-defect density and the capture cross section corresponding to the enhanced, nonradiative Shockley–Read–Hall (SRH) recombination at the GB plane and Φ_B is the barrier height that free charge carriers (electrons and holes) experience when approaching the GB. Although the ensemble of point defects differs from GB to GB and thus the net-charge density and consequently also Φ_B vary correspondingly, we assume that the effective SRH recombination described by the $N_{GB}\,\sigma_{GB}\,v_{th}$ term remains similar (within about the same order of magnitude). Thus, from the 20 different S_{GB} values, the median value $S_{GB,0}$ is calculated and identified with $N_{GB}\,\sigma_{GB}\,v_{th}$:$S_{GB}=S_{GB,0}\exp(-\Phi_B/k_BT)$.

$S_{GB,0}$ is the smallest for cell #4, whereas the $S_{GB,0}$ values of the cells #1, #2, #3, and #5 are all on the same order of few 100 cm/s.

1099159x, 2024, 12, Downloaded from https://onlinelibrary.wiley.com/doi/10.1002/pip.3845 by Helmholtz-Zentrum Berlin Für, Wiley Online Library on [12/12/2024]. See the Terms and Conditions (https://onlinelibrary.wiley.com/terms-and-conditions) on Wiley Online Library for rules of use; OA articles are governed by the applicable Creative Commons License

The CIGSe absorber of cell #2 with AAC = 0 exhibits the largest $S_{GB,0}$ value. The estimated values of τ_{eff}, τ_{bulk}, and τ_{GB} for all the CIGSe and ACIGSe absorbers are given in Table 3. It is evident that both τ_{bulk} and τ_{GB} of cell #2 are much smaller than those of cell #1, which correlates with the smaller d_{grain} and higher nonradiative V_{OC} loss $\Delta V_{OC}{}^{nonrad}$ of cell #2. τ_{GB} decreases from 710 to 100 ns from cell #3 to #5 with a corresponding increase in $\Delta V_{OC}{}^{nonrad}$ from 434 to 508 mV.

4 | Discussion

As evident from the results, various material properties such as the average grain size d_{grain}, the fluctuations in CL emission ($\sigma_{later.CL}/\sigma_{verti.CL}$), Ga/In gradients, the Urbach energy (E_u), and the electron lifetimes τ_{eff}, τ_{bulk}, and τ_{GB} have a substantial impact on the V_{OC} losses ΔV_{OC} of the solar cells. It is important to note that the effects of the Urbach energy are discussed below in connection with radiative V_{OC} losses; nevertheless, because Urbach tails are composed of defect levels, their impacts on nonradiative recombination and corresponding V_{OC} losses should not be neglected. In order to relate the material properties to the varying AAC and to the different origins of V_{OC} losses, it is convenient to group solar cells with identical E_g and discuss their radiative and nonradiative V_{OC} losses separately.

As mentioned above (Section 3), we are not able to conclude on CdS/(A)CIGSe interface properties in the present work; we would like to highlight the fact that with respect to the nonradiative V_{OC} losses discussed in the following subsections, enhanced nonradiative recombination at the CdS/(A)CIGSe interface can be expected to contribute to the given total V_{OC} losses (Table 1), in addition to the origins revealed by the techniques applied in the present work.

4.1 | Group 1 (Cells #1 and #2) With AAC = 0.05 and 0

Cells #1 and #2 exhibit a similar E_g of about 1.13–1.15 eV. Nevertheless, cell #2 features a higher ΔV_{OC} than that of cell #1. The $\Delta V_{OC}{}^{rad}$ of cell #1 (calculated from the absorption edge broadening, σ_{total}, via the approach in [9, 10]) is higher than that of cell #2. However, the CIGSe absorber of cell #2 exhibits a stronger Ga/In gradient owing to the absence of Ag in the absorber. Such pronounced local variation in composition induces considerable microstrain perpendicular to the substrate, thus leading to higher $\sigma_{verti.CL}$ in cell #2 than cell #1. Moreover, enhanced lateral fluctuations in the CL peak energy and larger E_U are in good agreement with additionally enhanced microstrain due to smaller average grain sizes for the CIGSe in cell #2, leading to correspondingly higher radiative V_{OC} losses.

The smaller average grain size of the CIGSe absorber of cell #2 (about 0.7 μm) as compared with that in the ACIGSe layer of cell #1 (about 1 μm) means also that the GB density in cell #2 is relatively higher—thus, more locations of enhanced nonradiative recombination. Moreover, the τ_{eff} in the CIGSe absorber in cell #2 is only about 60 ns, although cell #1 features an ACIGSe absorber with a τ_{eff} that is about twice as large. This trend also holds for the bulk and GB lifetimes. The GB recombination velocity ($S_{GB,0}$) is also larger for the CIGSe absorber in cell #2. These results indicate that owing to the absence of Ag in the CIGSe layer in cell #2, the average grain size d_{grain} is smaller, that is, the nonradiative recombination at GBs is enhanced as compared with that of cell #1, which contributes to the smaller τ_{eff} and thus to the higher ΔV_{OC}. This fact is also evident from the higher $\Delta V_{OC}{}^{nonrad}$ of cell #2.

Nonradiative V_{OC} losses exhibit a dominant contribution to the overall ΔV_{OC} in both cells, which is visible from the small differences between the τ_{GB} and $\tau_{eff,}$ values for each cell. The very high bulk lifetime for cell #1 indicates that defect-assisted (SRH) bulk recombination seems to be strongly reduced by the Ag alloying. We should note that recombination at the (A)CIGSe/Mo interface is not investigated in the present work; however, in spite of a stronger Ga/In gradient towards the CIGSe/Mo interface, the total ΔV_{OC} of cell #2 remains higher than cell #1. Thus, it can be assumed that there is not any significant effect of the corresponding back-surface fields on the V_{OC} loss of this cell. The impact of the Ag addition to a CIGSe absorber seems to be that the ACIGSe absorber exhibits larger d_{grain}, higher τ_{eff}, a flatter Ga/In gradient, and, consequently, a smaller ΔV_{OC}.

4.2 | Group 2 (Cells #3, #4, and #5) With $E_g \sim 1.2$ eV

The ACIGSe thin-film solar cells #3, #4, and #5 exhibit absorbers with a higher E_g of about 1.2 eV as compared with the cells in Group 1. However, the V_{OC} decreases steadily from cell #3 to #5, and also, an increase in the overall ΔV_{OC} from cells #3 to #5 is found. Even within the large grains of cell #3 (extending from CdS buffer to Mo back-contact) strong E_g gradients and local changes in the GGI ratios were identified within individual grains. However, due to the higher AAC of 0.14, the GGI

TABLE 3 | Estimated τ_{eff}, τ_{bulk}, and τ_{GB}, as well as the corresponding $\Delta V_{OC}{}^{nonrad}$ and E_g for all the five ACIGSe thin-film solar cells studied in the present work.

Cell no.	E_g (eV)	τ_{eff} (ns)	τ_{bulk} (ns)	$S_{GB,0}$ (cm/s)	$\tau_{GB} = d_{grain}/6S_{GB,0}$ (ns)	$\Delta V_{OC}{}^{nonrad}$ (mV)
#1	1.13	110	500	110	150	359
#2	1.15	60	170	190	60	380
#3	1.19	310	900	110	710	434
#4	1.20	250	500	40	330	458
#5	1.22	90	200	130	100	508

1099159x, 2024, 12, Downloaded from https://onlinelibrary.wiley.com/doi/10.1002/pip.3845 by Helmholtz-Zentrum Berlin Für, Wiley Online Library on [12/12/2024]. See the Terms and Conditions (https://onlinelibrary.wiley.com/terms-and-conditions) on Wiley Online Library for rules of use; OA articles are governed by the applicable Creative Commons License

gradients in the ACIGSe absorbers in cells #3 and #5 are slightly less pronounced than the one in the absorber of cell #4. This difference in the E_g or GGI gradient is well evident in the σ_{total} of these cells. Cell #4 with the most pronounced GGI gradient exhibits the highest σ_{total} and, correspondingly, the largest ΔV_{OC}^{rad} among the three cells. In all these ACIGSe absorbers, $\sigma_{verti.CL}$ remains much higher than $\sigma_{later.CL}$, probably owing to the strain induced by the Ga/In gradients.

Additional origins for radiative V_{OC} losses are indicated, as also found and discussed in Section 4.1, by the quantities $\sigma_{later.CL}$, $\sigma_{verti.CL}$, and E_U. Additional strain due to structural changes indicated by $|c/a-2|$ leads to higher E_U and also to higher σ_{total} values—thus to higher radiative V_{OC} losses. In the case of cell #3 with a very large average grain size of almost 5 μm, the correspondingly small GB density is counterbalanced by a high $|c/a-2|$ value, still resulting in substantial residual strain in the absorber, as indicated by the $\sigma_{later.CL}$ value that is similar to those for cells #4 and #5. The ACIGSe absorber of cell #5 with the largest E_U and $\sigma_{verti:CL}$ also exhibits the highest deviation from the pseudocubic point. Thus, cell #5 is more likely to exhibit larger radiative V_{OC} losses due to enhanced recombination via extended defect states.

The ACIGSe absorber of cell #3 features the same AAC as cell #5 but much larger d_{grain} of about 4.7 μm (cells #5: $d_{grain} = 0.8\,\mu m$) due to the higher substrate temperature during the synthesis of 650°C vs. 580°C and in part also due to the higher GGI and the lower ACGI of cell #5. As the GB density is smaller in the absorber of cell #3, it seems consequent that for this cell, the τ_{eff} and τ_{GB} values in the ACIGSe absorber of 310 and 710 ns are also the largest among the three cells. However, the GB recombination velocity ($S_{GB,0}$) of this cell is higher than that of cell #4. This result shows that $S_{GB,0}$ is not linked directly to the AAC ratio of the absorber. The steady decrease in τ_{eff}, τ_{bulk}, and τ_{GB} from cell #3 to cell #5 correlates well with their decreasing V_{OC}, which can be understood since the V_{OC} is proportional to τ_{eff} [35].

The τ_{eff}, τ_{bulk}, and τ_{GB} values decrease from cells #3 to #5. It is evident that the differences in the electron lifetimes are dominant contributions to the V_{OC} losses of these cells. These V_{OC} losses can originate from factors such as recombination in the bulk and from ACIGSe/Mo interface recombination in addition to the recombination at the GBs. As cells #4 and #5 exhibit a higher GGI towards the ACIGSe/Mo interface, a favorable impact on their V_{OC} losses from the back-surface field can be expected. A higher ΔV_{OC} of cells #4 and #5 may be due to a smaller ACGI in the absorber layers of these cells. In addition to the variation in Ag and Cu in the present case, a pronounced Ga/In gradient in the ACIGSe absorber does not seem to improve the device performance. In cell #5, similar τ_{GB} and τ_{eff} values indicate that the effective lifetime of the electrons is limited by their lifetime at the GBs. Thus, the enhanced nonradiative recombination at the GBs has a major effect on its overall ΔV_{OC}.

5 | Conclusions

In the present work, the effect of Ag addition on the microstructure–property relationships in (A)CIGSe thin-film solar cells was investigated. Various microscopic and macroscopic materials properties of (A)CIGSe absorber layers with similar E_g values but with different V_{OC} deficits were studied. Considerable Ga/In gradients were present in all (A)CIGSe absorbers, leading to radiative V_{OC} losses in the corresponding devices. Moreover, the effective lifetime of the electrons in the absorbers are limited mainly by the lifetime at the GBs, indicating that nonradiative recombination of charge carriers at GBs is a major contribution to the nonradiative V_{OC} deficits of the (A)CIGSe thin-film solar cells. ACIGSe absorbers with high effective electron lifetimes of larger than 100 ns can be obtained via increase of the average grain sizes to larger than 1 μm. In order to achieve enhanced device performances of the thin-film solar cells, the ACIGSe absorbers must be grown with very flat Ga/In gradients throughout the absorber except for a strong increase towards the back-contact (for an efficient back-surface field), with larger grains (several μm), and with a composition appropriate for a pseudocubic crystal structure.

Acknowledgments

The authors are grateful to Ulrike Bloeck (HZB) for assistance with the cross-sectional specimen preparation for SEM. The present work was supported by the Graduate School "MatSEC" and the "EFFCIS-II" under contract numbers 03EE1059A (ZSW), 03EE1059B (HZB), and 03EE1059C (MLU). Open Access funding enabled and organized by Projekt DEAL.

Author Contribution

Sinju Thomas: main author, microscopic analyses. **Wolfram Witte:** sample preparation, writing. **Dimitrios Hariskos:** sample preparation, writing. **Rico Gutzler:** sample preparation, writing. **Stefan Paetel:** sample preparation, writing. **Chang-Yun Song:** TRPL analysis, writing. **Heiko Kempa:** TRPL analysis, writing. **Matthias Maiberg:** TRPL analysis, writing. **Daniel Abou-Ras:** corresponding author, supervision of the work

Conflicts of Interest

The authors declare no conflicts of interest.

Data Availability Statement

The raw data of the present work are available with the corresponding author upon request.

References

1. J. Keller, K. Kiselman, O. Donzel-Gargand, et al., "High-Concentration Silver Alloying and Steep Back-Contact Gallium Grading Enabling Copper Indium Gallium Selenide Solar Cell With 23.6% Efficiency," *Nature Energy* 9 (2024): 467–478, https://doi.org/10.1038/s41560-024-01472-3.

2. P. Erslev, G. M. Hanket, W. N. Shafarman, and D. J. Cohen, "Characterizing the Effects of Silver Alloying in Chalcopyrite CIGS With Junction Capacitance Methods," *MRS Proceedings* 1165 (2009): 1165-M01-07, https://doi.org/10.1557/PROC-1165-M01-07.

3. L. Chen, J. Lee, and W. N. Shafarman, "The Comparison of (Ag,Cu)(In,Ga)Se_2 and Cu (In,Ga)Se_2 Thin Films Deposited by Three-Stage Coevaporation," *IEEE Journal of Photovoltaics* 4, no. 1 (2014): 447–451, https://doi.org/10.1109/JPHOTOV.2013.2280471.

4. J. H. Boyle, B. E. McCandless, W. N. Shafarman, and R. W. Birkmire, "Structural and Optical Properties of (Ag,Cu)(In,Ga)Se_2 Polycrystalline Thin Film Alloys," *Journal of Applied Physics* 115, no. 22 (2014): 223504, https://doi.org/10.1063/1.4880243.

1099159x, 2024, 12, Downloaded from https://onlinelibrary.wiley.com/doi/10.1002/pip.3845 by Helmholtz-Zentrum Berlin Für, Wiley Online Library on [12/12/2024]. See the Terms and Conditions (https://onlinelibrary.wiley.com/terms-and-conditions) on Wiley Online Library for rules of use; OA articles are governed by the applicable Creative Commons License

5. K. Kim, J. W. Park, J. S. Yoo, J. Cho, H.-D. Lee, and J. H. Yun, "Ag Incorporation in Low-Temperature Grown Cu(In,Ga)Se_2 Solar Cells Using Ag Precursor Layers," *Solar Energy Materials and Solar Cells* 146 (2016): 114–120, https://doi.org/10.1016/j.solmat.2015.11.028.

6. C. P. Thompson, Lei Chen, W. N. Shafarman, Jinwoo Lee, S. Fields, and R. W. Birkmire, "Bandgap Gradients in (Ag,Cu)(In,Ga)Se_2 Thin Film Solar Cells Deposited by Three-Stage co-Evaporation," in *2015 IEEE 42nd Photovoltaic Specialist Conference (PVSC)* (New Orleans, LA: IEEE, 2015): 1–6, https://doi.org/10.1109/PVSC.2015.7355692.

7. R. Gutzler, W. Witte, A. Kanevce, D. Hariskos, and S. Paetel, "V_{oc} -Losses Across the Band Gap: Insights From a High-Throughput Inline Process for CIGS Solar Cells," *Progress in Photovoltaics* 31, no. 10 (2023): 1023–1031, https://doi.org/10.1002/pip.3707.

8. J. T. Heath, J. D. Cohen, and W. N. Shafarman, "Bulk and Metastable Defects in $CuIn_{1-x}Ga_xSe_2$ Thin Films Using Drive-Level Capacitance Profiling," *Journal of Applied Physics* 95, no. 3 (2004): 1000–1010, https://doi.org/10.1063/1.1633982.

9. U. Rau, B. Blank, T. C. M. Müller, and T. Kirchartz, "Efficiency Potential of Photovoltaic Materials and Devices Unveiled by Detailed-Balance Analysis," *Physical Review Applied* 7, no. 4 (2017): 044016, https://doi.org/10.1103/PhysRevApplied.7.044016.

10. U. Rau and J. H. Werner, "Radiative Efficiency Limits of Solar Cells With Lateral Band-Gap Fluctuations," *Applied Physics Letters* 84, no. 19 (2004): 3735–3737, https://doi.org/10.1063/1.1737071.

11. M. Troviano and K. Taretto, "Urbach Energy in CIGS Extracted From Quantum Efficiency Analysis of High Performance CIGS Solar Cells," in *24th European Photovoltaic Solar Energy Conference*, 21–25 September 2009, (2009), https://doi.org/10.4229/24THEUPVSEC2009-3BV.5.22.

12. D. Abou-Ras, U. Bloeck, S. Caicedo-Dávila, et al., "Correlative Microscopy and Monitoring of Segregation Processes in Optoelectronic Semiconductor Materials and Devices," *Journal of Applied Physics* 133, no. 12 (2023): 121101, https://doi.org/10.1063/5.0138952.

13. W. Shockley and H. J. Queisser, "Detailed Balance Limit of Efficiency of *p-n* Junction Solar Cells," *Journal of Applied Physics* 32, no. 3 (1961): 510–519, https://doi.org/10.1063/1.1736034.

14. P. T. Erslev, J. Lee, G. M. Hanket, W. N. Shafarman, and J. D. Cohen, "The Electronic Structure of Cu($In_{1-x}Ga_x$)Se_2 Alloyed With Silver," *Thin Solid Films* 519, no. 21 (2011): 7296–7299, https://doi.org/10.1016/j.tsf.2011.01.368.

15. P. Pearson, J. Keller, L. Stolt, and C. Platzer Björkman, "Investigating the Role of Ag and Ga Content in the Stability of Wide-Gap (Ag,Cu)(In,Ga)Se_2 Thin-Film Solar Cells," *Physica Status Solidi B* 260, no. 7 (2023): 2300170, https://doi.org/10.1002/pssb.202300170.

16. D. Abou-Ras, S. Schorr, and H. W. Schock, "Grain-Size Distributions and Grain Boundaries of Chalcopyrite-Type Thin Films," *Journal of Applied Crystallography* 40, no. 5 (2007): 841–848, https://doi.org/10.1107/S0021889807032220.

17. K. V. Sopiha, J. K. Larsen, O. Donzel-Gargand, et al., "Thermodynamic Stability, Phase Separation and Ag Grading in (Ag,Cu)(In,Ga)Se_2 Solar Absorbers," *Journal of Materials Chemistry A* 8, no. 17 (2020): 8740–8751, https://doi.org/10.1039/D0TA00363H.

18. S. C. Abrahams and J. L. Bernstein, "Piezoelectric Nonlinear Optic CuGaS2 and CuInS2 Crystal Structure: Sublattice Distortion in AIBIIIC2VI and AIIBIVC2V Type Chalcopyrites," *Journal of Chemical Physics* 59, no. 10 (1973): 5415–5422, https://doi.org/10.1063/1.1679891.

19. K. S. Knight, "The Crystal Structures of $CuInSe_2$ and $CuInTe_2$," *Materials Research Bulletin* 27, no. 2 (1992): 161–167, https://doi.org/10.1016/0025-5408(92)90209-I.

20. Y. Zhu, B. Wei, J. Liu, et al., "Physical Insights on the Low Lattice Thermal Conductivity of $AgInSe_2$," *Materials Today Physics* 19 (2021): 100428, https://doi.org/10.1016/j.mtphys.2021.100428.

21. P. Benoit, P. Charpin, R. Lesueur, and C. Djega-Mariadassou, "Crystal Structure of Chalcopyrite $AgInSe_2$," *Japanese Journal of Applied Physics* 19, no. S3 (1980): 85, https://doi.org/10.7567/JJAPS.19S3.85.

22. S.-H. Wei, S. B. Zhang, and A. Zunger, "Effects of Ga Addition to $CuInSe_2$ on Its Electronic, Structural, and Defect Properties," *Applied Physics Letters* 72, no. 24 (1998): 3199–3201, https://doi.org/10.1063/1.121548.

23. S. Thomas, T. Bertram, C. Kaufmann, et al., "Effects of Material Properties of Band-Gap-Graded Cu (In,Ga)Se_2 Thin Films on the Onset of the Quantum Efficiency Spectra of Corresponding Solar Cells," *Progress in Photovoltaics* 30, no. 10 (2022): 1238–1246, https://doi.org/10.1002/pip.3572.

24. B. G. Mendis, L. Bowen, and Q. Z. Jiang, "A Contactless Method for Measuring the Recombination Velocity of an Individual Grain Boundary in Thin-Film Photovoltaics," *Applied Physics Letters* 97, no. 9 (2010): 092112, https://doi.org/10.1063/1.3486482.

25. M. Krause, A. Nikolaeva, M. Maiberg, et al., "Microscopic Origins of Performance Losses in Highly Efficient Cu(In,Ga)Se_2 Thin-Film Solar Cells," *Nature Communications* 11, no. 1 (2020): 4189, https://doi.org/10.1038/s41467-020-17507-8.

26. D. Abou-Ras, A. Nikolaeva, M. Krause, et al., "Optoelectronic Inactivity of Dislocations in Cu (In,Ga)Se_2 Thin Films," *Physica Status Solidi RRL: Rapid Research Letters* 15, no. 7 (2021): 2100042, https://doi.org/10.1002/pssr.202100042.

27. S. Thomas, W. Witte, D. Hariskos, et al., "Effect of Ga variation on the bulk and grain-boundary properties of Cu (In,Ga)Se_2 absorbers in thin-film solar cells and their impacts on open-circuit voltage losses," *Progress in Photovoltaics* (2023), https://doi.org/10.1002/pip.3843.

28. W. K. Metzger, I. L. Repins, M. Romero, et al., "Recombination Kinetics and Stability in Polycrystalline Cu (In,Ga)Se_2 Solar Cells," *Thin Solid Films* 517, no. 7 (2009): 2360–2364, https://doi.org/10.1016/j.tsf.2008.11.050.

29. J. Bass, "Deviations From Matthiessen's Rule," *Advances in Physics* 21, no. 91 (1972): 431–604, https://doi.org/10.1080/00018737200101308.

30. M. Maiberg, T. Hölscher, S. Zahedi-Azad, and R. Scheer, "Theoretical Study of Time-Resolved Luminescence in Semiconductors. III. Trap States in the Band Gap," *Journal of Applied Physics* 118, no. 10 (2015): 105701, https://doi.org/10.1063/1.4929877.

31. A. B. Sproul, "Dimensionless Solution of the Equation Describing the Effect of Surface Recombination on Carrier Decay in Semiconductors," *Journal of Applied Physics* 76, no. 5 (1994): 2851–2854, https://doi.org/10.1063/1.357521.

32. R. K. Ahrenkiel and J. Dashdorj, "Interface Recombination Velocity Measurement by a Contactless Microwave Technique," *Journal of Vacuum Science & Technology, B: Microelectronics and Nanometer Structures–Processing, Measurement, and Phenomena* 22, no. 4 (2004): 2063–2067, https://doi.org/10.1116/1.1768523.

33. J. Li, J. Huang, F. Ma, et al., "Unveiling Microscopic Carrier Loss Mechanisms in 12% Efficient $Cu_2ZnSnSe_4$ Solar Cells," *Nature Energy* 7, no. 8 (2022): 754–764, https://doi.org/10.1038/s41560-022-01078-7.

34. J. A. Quirk, M. U. Rothmann, W. Li, D. Abou-Ras, and K. P. McKenna, "Grain Boundaries in Polycrystalline Materials for Energy Applications: First Principles Modeling and Electron Microscopy," *Applied Physics Reviews* 11 (2024): 011308.

35. B. J. Stanbery, D. Abou-Ras, A. Yamada, and L. Mansfield, "CIGS Photovoltaics: Reviewing an Evolving Paradigm," *Journal of Physics D: Applied Physics* 55, no. 17 (2022): 173001, https://doi.org/10.1088/1361-6463/ac4363.

Supporting Information

Additional supporting information can be found online in the Supporting Information section.

1099159x, 2024, 12, Downloaded from https://onlinelibrary.wiley.com/doi/10.1002/pip.3845 by Helmholtz-Zentrum Berlin Für, Wiley Online Library on [12/12/2024]. See the Terms and Conditions (https://onlinelibrary.wiley.com/terms-and-conditions) on Wiley Online Library for rules of use; OA articles are governed by the applicable Creative Commons License